PAPER

Check for updates

Ultrafine ZnCo$_2$O$_4$ QD-incorporated carbon nitride mediated peroxymonosulfate activation for norfloxacin oxidation: performance, mechanisms and pathways†

Tao Zeng, [ID] *[ab] Sijia Jin,[b] Zhiquan Jin,[b] Shuqi Li,[bc] Rui Zou,[b] Xiaole Zhang, [ID] [d] Shuang Song [ID] [b] and Min Liu*[a]

Recently, peroxymonosulfate (PMS)-based advanced oxidation processes (AOPs) are being actively investigated as a potential technology for water decontamination and many efforts have been made to improve the activation efficiency of PMS. Herein, a 0D metal oxide quantum dot (QD)–2D ultrathin g-C$_3$N$_4$ nanosheet (ZnCo$_2$O$_4$/g-C$_3$N$_4$) hybrid was facilely fabricated through a one-pot hydrothermal process and used as an efficient PMS activator. Benefiting from the restricted growth effect of the g-C$_3$N$_4$ support, ultrafine ZnCo$_2$O$_4$ QDs ($\sim$3–5 nm) are uniformly and stably anchored onto the surface. The ultrafine ZnCo$_2$O$_4$ possesses high specific surface areas and shortened mass/electron transport route so that the internal static electric field ($E_{internal}$) formed in the interface between p-type ZnCo$_2$O$_4$ and the n-type g-C$_3$N$_4$ semiconductor could speed up the electron transfer during the catalytic reaction. This thereby induces the high-efficiency PMS activation for rapid organic pollutant removal. As expected, the ZnCo$_2$O$_4$/g-C$_3$N$_4$ hybrid catalysts significantly outperformed individual ZnCo$_2$O$_4$ and g-C$_3$N$_4$ in catalytic oxidative degradation of norfloxacin (NOR) in the presence of PMS (95.3% removal of 20 mg L^{-1} of NOR in 120 min). Furthermore, the ZnCo$_2$O$_4$/g-C$_3$N$_4$-mediated PMS activation system was systematically studied in terms of the identification of reactive radicals, the impact of control factors, and the recyclability of the catalyst. The results of this study demonstrated the great potential of a built-in electric field-driven catalyst as a novel PMS activator for the remediation of contaminated water.

1. Introduction

Contamination of water with antibiotics has attracted increased attention due to the environmental and public health concerns.[1] As synthetic broad-spectrum antibiotics, fluoroquinolones have been utilized more frequently to manage bacterial infections in human beings, livestock, and aquaculture. Norfloxacin (NOR) is one of the most commonly discovered fluoroquinolones in drinking water, surface water, and wastewater on a worldwide scale attributable to the poor capacity of traditional sewage treatment procedures to remove

antibiotics.[2] Although the concentration of NOR detection varies from ng L^{-1} to g L^{-1} in aquatic environments, the negative health consequences on aquatic biota at various trophic levels owing to the continuous input and bio-accumulation make it categorized as an emerging pseudo-persistent pollutant.[3] Numerous techniques, such as adsorption,[4] biodegradation,[5] and ultrafiltration,[6] have been examined for their NOR removal potential. Nevertheless, low removal efficiency and slow reaction rate impede their practical application. By contrast, catalytic technology[7–12] is an essential high-tech and green environmental protection technology, providing immense economic and social benefits while being a crucial factor in the advancement of the chemical industry and society.

Recently, sulfate radical (SO$_4^{\cdot-}$)-based advanced oxidation processes (AOPs) particularly have been taken into consideration as an efficient and promising technology in terms of complete decomposition of antibiotics in a short time by producing radicals. In comparison to hydroxyl radicals ($^{\cdot}$OH, 1.8–2.7 V), SO$_4^{\cdot-}$ has higher redox potential (2.5–3.1 V) and longer lifetime with more flexible pH requirement, thus allowing the effective reaction with the target organic pollutants.[13,14] Anipsitakis and Dionysiou[15] found that cobalt ions (Co^{2+})

[a]College of Architecture and Environment, Sichuan University, Sichuan 610065, China. E-mail: zengtao@zjut.edu.cn; liuminscu@163.com; Tel: +86-571-88320726

[b]Key Laboratory of Microbial Technology for Industrial Pollution Control of Zhejiang Province, College of Environment, Zhejiang University of Technology, Hangzhou, Zhejiang 310032, P. R. China

[c]Hangzhou Vocational & Technical College, Ecology and Health Institute, Hangzhou, 310018, P. R. China

[d]College of Life Science, North China University of Science and Technology, Tangshan, Hebei, 063000, China. E-mail: smilxin@126.com

† Electronic supplementary information (ESI) available. See DOI: https://doi.org/10.1039/d3ra02364h

exhibited the highest ability to activate peroxymonosulfate (PMS) for $SO_4^{\cdot-}$ generation and cobalt oxide (Co_3O_4) was effective in heterogeneously PMS activation. However, considering that cobalt is both toxic and somewhat expensive, efforts are underway to replace Co_3O_4 with more environmentally benign and inexpensive alternative metals.

$ZnCo_2O_4$, which is isostructural to Co_3O_4, is a typical spinel with the Co^{3+} occupying the octahedral sites and the Zn^{2+} filling the tetrahedral sites in the cubic spinel structure. The replacement of Co^{2+} by Zn^{2+} may not only facilitate the PMS activation but also suppress Co leaching due to the strong Zn–Co interactions, which renders $ZnCo_2O_4$ to be a promising candidate for PMS activation.[16–18] While there is still a considerable problem to be solved for substantially improving the catalytic performance and the stability of current catalysts. For instance, ultrafine nanoscale metal oxides usually provide high specific surface areas as well as reduced mass/electron transfer pathway, which are highly beneficial for catalytic processes.[19–21] But individual nanoparticles (NPs) unavoidably likely to aggregate during the operation attribute to the high surface energy, leading to the decrease of the catalytic activity.[22] A manageable synthesis method for ultrafine nanoscale PMS activators is therefore urgently needed.

To alleviate the agglomeration of ultrafine $ZnCo_2O_4$ NPs, support effects can be imaginably utilized to improve their dispersion over the surface of catalyst. In recent years, a variety of catalyst supports, such as metal oxides,[23] graphene,[24] and metal–organic frameworks,[25] have all been employed to stabilize NPs,[26,27] which endows the resultant hybrids with increased catalytic activity for antibiotic degradation. In addition, many researchers have also been encouraged to study the synergistic effect between the metal nanoparticles and catalyst support.[28–31] Among the majority of available supports, graphitic carbon nitride (g-C_3N_4), with inexpensive materials and high stability for simple preparation, has prominent advantages in embedding NPs.[32–35] The high affinity of the organic moieties of g-C_3N_4 toward transition metal species contribute to achieving the strong coupling between g-C_3N_4 and $ZnCo_2O_4$ NPs. Furthermore, the difference in electronegativity between N and C atoms could cause a significantly positive charge on neighboring C, facilitating PMS adsorption. More importantly, by integrating p-type semiconductor $ZnCo_2O_4$ with n-type semiconductor g-C_3N_4, a p–n heterojunction interface could be formed because of their favorable band alignment, which leads to the creation of an internal electric field to accelerate the interfacial electron transfer.[36]

With these in mind, we herein report the construction of an effective built-in electric field-driven catalyst system based on multifunctional g-C_3N_4 supported ultrasmall $ZnCo_2O_4$ quantum dots (QDs) for enhanced degradation of NOR in the presence of PMS. Besides the merits mentioned above, the g-C_3N_4 support was also able to restrict the $ZnCo_2O_4$ NPs growth, thus allowing stabilization of the smaller NPs with higher chemical reactivity. The effects of catalyst dosage, NOC and PMS concentration, and pH value on NOR removal were evaluated in details. The reaction mechanism as well as the degradation pathway of NOR was also investigated. As a green oxidation process, the activation of PMS with this built-in electric field-driven $ZnCo_2O_4$/g-C_3N_4 catalyst is a valuable, promising, and viable method for antibiotics-contaminated wastewater treatment.

2. Material and methods (experimental section)

2.1 Materials

Target contaminant of norfloxacin ($C_{16}H_{18}FN_3O_3$ 98% in purity) was purchased from J&K Chemical Ltd. Other chemicals used for synthesizing $ZnCo_2O_4$ and g-C_3N_4, such as cobalt acetate ($Co(CH_3COO)_3\cdot4H_2O$), dicyandiamide ($C_2H_4N_4$), ammonium chloride (NH_4Cl) and zinc acetate ($Zn(CH_3COO)_2\cdot2H_2O$), ammonium hydroxide ($NH_3\cdot H_2O$, 25–28% NH_3), concentrated hydrochloric acid (HCl, 36–38%, w/v), and anhydrous ethanol (C_2H_6O) were supplied by J&K Chemical Ltd. Potassium peroxymonosulfate ($2KHSO_5\cdot KHSO_4\cdot K_2SO_4$, PMS) was purchased from Sigma-Aldrich. Sodium hydroxide (NaOH), potassium iodide (KI), and *tert*-butyl alcohol (TBA) were obtained from Huadong Medicine Co., Ltd. No further purification was performed on any of the compounds.

2.2 Synthesis of the catalysts

2.2.1 Preparation of g-C_3N_4.
A modified "bottom-up" dicyandiamide-blowing strategy was used to prepare g-C_3N_4 nanosheets. Briefly, the mixture of 3.0 g of dicyandiamide and 30 g of NH_4Cl was put into the crucible, and heated to 550 °C, then held for 4 h in air atmosphere. After being cooled down naturally, the samples were repetitively washed with 5% HCl solution and double-distilled water in an ultrasound bath, followed by lyophilization.

2.2.2 Preparation of $ZnCo_2O_4$/g-C_3N_4 heterojunction and sole $ZnCo_2O_4$ NPs.
After acid treatment, 0.068 g of the as-prepared g-C_3N_4 was dispersed in a mixed liquor containing 4.0 mL of deionized water and 96 mL of ethanol, followed by the addition of 0.319 g of $Co(CH_3COO)_3\cdot4H_2O$ and 0.141 g of $Zn(CH_3COO)_2\cdot2H_2O$ to the suspension successively. Subsequently, 1.0 mL of $NH_3\cdot H_2O$ was injected dropwise at room temperature and the suspension was rapidly agitated with a magnetic stirrer at 300 rpm in an 80 °C water bath for 20 h. Finally, the mixture for the reaction was put into to a 100 mL autoclave and heated to 150 °C for three hours to begin the hydrothermal reaction. The finished product was centrifuged, cleaned with ethanol and deionized water, then lyophilized for drying.

The sole $ZnCo_2O_4$ NPs without g-C_3N_4 support was synthesized utilizing the same approach as described above except for the addition of g-C_3N_4.

2.3 Catalyst characterization

The crystal phases of the as-prepared samples were recorded by X-ray diffractometry (XRD, X'Pert PRO MPD, PANalytical, Netherlands) using Cu Kα radiation ($\lambda = 1.540562$ Å) over a 2θ range of 10–80°. The morphology features and microstructures of the catalysts were characterized by field-emission scanning

electron microscopy (FE-SEM, S-4800, Hitachi, Japan) and high-resolution transmission electron microscopy (HRTEM, FEI Tecnai G2 F30, FEI, Holland). X-ray photoelectron spectroscopy (XPS, PHI 5000C ESCA, PerkinElmer, USA) was applied to analyze the composition and the valence state of the specimens. The specific surface area was calculated using the N_2 adsorption–desorption isotherms (BET, ASAP2010, Micromeritics, USA). Fourier transform infrared spectra were recorded on a spectrophotometer (FT-IR, VERTEX 70, Bruker, Germany) in KBr pellets to recognize the functional groups. Thermogravimetric analysis (TGA, DTG-60h, Shimadzu, Japan) was applied within a temperature range of 25–800 °C at a rate of 10 °C per minute under static N_2 atmosphere to test the thermal stability of the samples. Atomic absorption spectrophotometer (AAS, Shimadzu, Japan) was used for detecting the ion-leaching of Zn, Co from the samples.

2.4 Catalytic activity test and sample analysis

The catalytic activity tests were conducted in a shaking table with a rotation speed of 250 rpm at atmospheric pressure. In a typical run, the catalysts (0.2 g L^{-1}) and PMS (0.15 mM) were added to a 0.06 mM NOR aqueous solution without light irradiation. At preset intervals, 1.0 mL of the reaction mixture was withdrawn, quenched with excess methanol and centrifuged. In a single factor effect experiment, we keep all other conditions constant while only altering one factor condition, such as catalyst concentration, PMS concentration, pollutant solution concentration, pH, and temperature to study the impact of the change on the degradation performance. The concentrations of NOR in the supernatant were analyzed by high performance liquid chromatography (HPLC, LC-1200, Agilent, USA) equipped with a C18 column (150 mm × 4.6 mm × 5 μm, Eclipse XDB-C18, Agilent, USA) and a UV detector at $\lambda = 278$ nm. The column temperature was held at 30 °C, while the mobile phase was formic acid–water–acetonitrile (0.002 : 30 : 70) with a flow rate of 0.3 mL min^{-1} and a 10 μL injection volume.

The NOR intermediates/products during reaction process were quantitated on a Waters ACQUITY UPLC-MS/MS system with triple quadrupole mass spectrometer XEVO TQ MS (Waters, Milford, MA, USA) in positive ion mode controlled by Waters Mass Lynx software. For chromatographic separation, the ACQUITY UPLC® BEH C18 column (50 mm × 2.1 mm × 1.7 μm) was used when the column temperature is 35 °C. The mobile phase was consisted of acetonitrile (A) and 0.2% formic acid (B). The solvents were set at a flow rate of 0.2 mL min^{-1} in the gradient mode (0 min, 5% A; 5 min, 5% A; 10 min, 10% A; 15 min, 10% A; 18 min, 15% A; 30 min, 25% A; 35 min, 25% A; 45 min, 5% A; 50 min, 5% A). MS spectra were obtained through a full scan mode (m/z 50 to 500).

The samples were collected and washed by ethanol and deionized water several times after 2 hours of reactions, and then freeze-dried in a lyophilizer for reuse. The cyclic experiment followed the same procedure mentioned above.

3. Results and discussion

3.1 Catalyst characterization

The $ZnCo_2O_4$ QDs were formed and anchored onto the g-C_3N_4 surface by a facile one-pot hydrothermal process for producing the hybrid catalyst $ZnCo_2O_4$/g-C_3N_4. The morphology and structure of g-C_3N_4, $ZnCo_2O_4$ and $ZnCo_2O_4$/g-C_3N_4 were illustrated by SEM and TEM. As displayed in Fig. 1a, individual $ZnCo_2O_4$ NPs, with a diameter of ∼20 nm, aggregate severely because of the high surface energy.[37] Pure g-C_3N_4 appears as
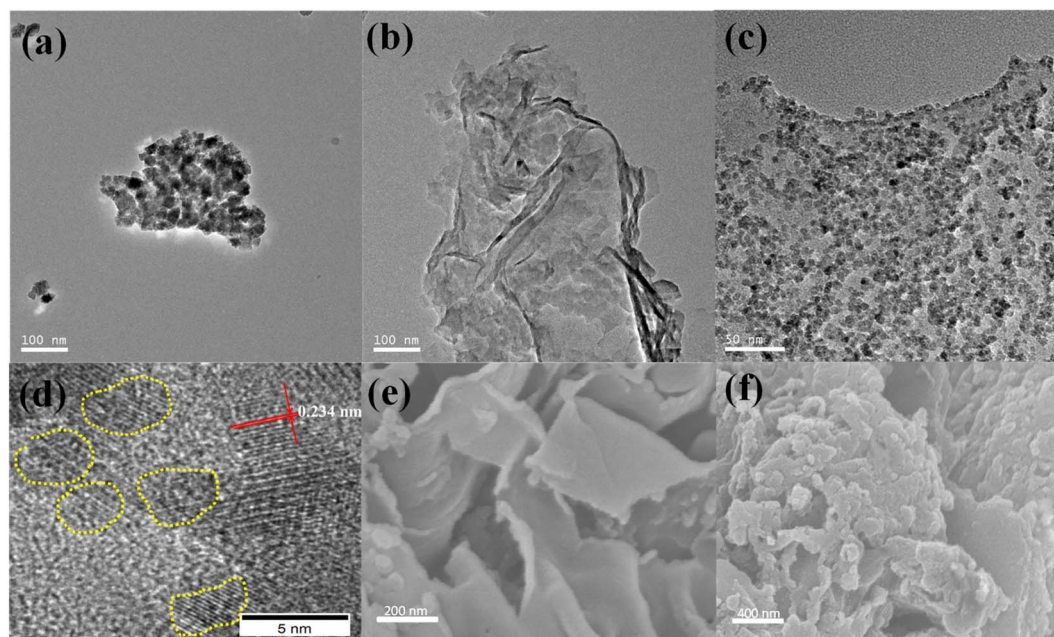

Fig. 1 TEM images of (a) $ZnCo_2O_4$, (b) g-C_3N_4, (c) $ZnCo_2O_4$/g-C_3N_4; (d) HRTEM image of $ZnCo_2O_4$/g-C_3N_4; and SEM images of (e) g-C_3N_4 and (f) $ZnCo_2O_4$/g-C_3N_4.

layered structure with wrinkled planes, suggesting the thin and flexible feature of the nanosheets (Fig. 1b). For the $ZnCo_2O_4$/g-C_3N_4 composites (Fig. 1c), it can be observed that the g-C_3N_4 nanosheet was covered by $ZnCo_2O_4$ QDs and no unbounded nanoparticles was found. It is worth noting that the particle size of $ZnCo_2O_4$ (Fig. S1†) is significantly decreased to around 3–6 nm, as compared with the individual ones, which may be originated from the support effect of g-C_3N_4. The high-resolution TEM image (Fig. 1d) further confirms the good anchor-hold between $ZnCo_2O_4$ QDs and g-C_3N_4. The lattice spacing in the heterojunction is determined to be 0.234 nm, attributing to the (222) crystal plane of $ZnCo_2O_4$,[38] which can also be verified by the strongest diffraction peak of the next X-ray diffraction results. However, the lattice fringe of g-C_3N_4 cannot be observed probably due to its weak crystallization. More specifically, the robust coupling of N groups toward transition Zn^{2+} and Co^{2+} ions not only stabilized the highly dispersed $ZnCo_2O_4$ NPs but also controled the nucleation to form uniform QDs. The SEM image of g-C_3N_4 (Fig. 1e) displayed a smooth flake appearance with an average diameter of 0.5–1.0 μm, while the $ZnCo_2O_4$/g-C_3N_4 sample presented a relatively rougher surface (Fig. 1f), which is basically consistent with the results in TEM. To gain insights into the elemental distribution of the $ZnCo_2O_4$/g-C_3N_4 hybrids, EDS-elemental mapping analysis (Fig. S2†) was conducted, and the results indicated the homogeneous distribution of C, N, O, Co, and Zn elements in the sheets.

XRD technique was used to dissect the structural phase of the materials. In Fig. 2a, the peaks at 2θ of 13.0° and 27.5° are demonstrated to be characteristic of the g-C_3N_4 (100) and (002) reflection (JCPDS no. 87-1526).[39] The pattern of individual $ZnCo_2O_4$ exhibits peaks at 2θ of 18.9°, 31.2°, 36.8°, 38.5°, 44.7°, 55.6°, 59.3°, 65.2°, 77.2°, and 78.3°, corresponding to the (111), (220), (311), (222), (400), (422), (511), (440), (533), and (622) planes of $ZnCo_2O_4$ (JCPDS no. 023-1390).[18] Due to the abundant $ZnCo_2O_4$ QDs covering the g-C_3N_4 surface in the $ZnCo_2O_4$/g-C_3N_4 samples, all the original diffraction peaks of g-C_3N_4 except the sharpest peak at 26.5° disappeared. These observations further elucidate the successful formation of $ZnCo_2O_4$/g-C_3N_4 materials.

The porous structure and surface area of the nanocomposites can be well investigated from its N_2 adsorption–desorption isotherms. Fig. 2b shows that all the isotherms of g-C_3N_4, $ZnCo_2O_4$, and $ZnCo_2O_4$/g-C_3N_4 have the type IV curve with a type H3 hysteresis loop, suggesting the mesoporous structure of the catalysts. The BET specific surface area of $ZnCo_2O_4$/g-C_3N_4 is 92.18 m^2 g^{-1}, which is slightly higher than those of $ZnCo_2O_4$ (82.03 m^2 g^{-1}) and g-C_3N_4 (69.39 m^2 g^{-1}) counterparts. High surface area may endow the catalysts with more active sites and thus enhances the adsorption of reactant species. The thermal stability of the samples was examined *via* the TG technique. As demonstrated in Fig. 2c, adsorbed solvent molecules may have evaporated at temperatures below 100 °C, causing the first weight loss in all sample.[40] In the curve of pure
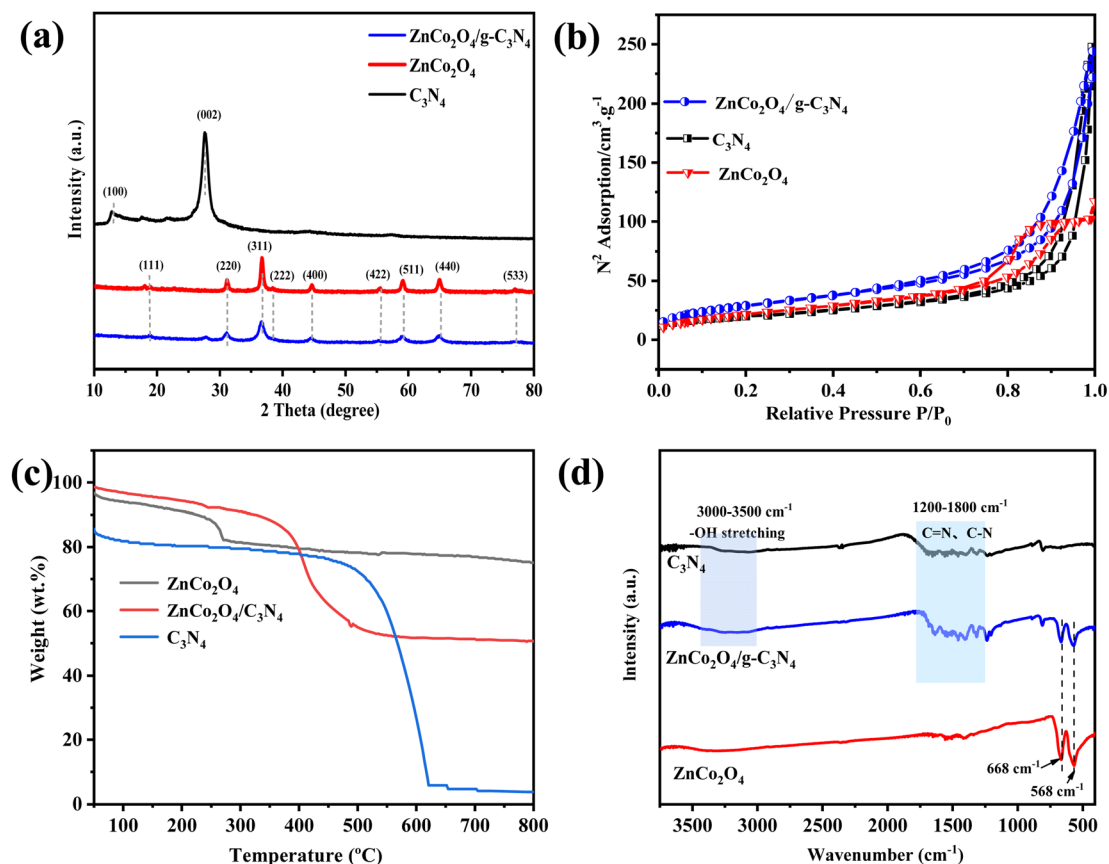

Fig. 2 (a) XRD patterns. (b) N_2 adsorption–desorption isotherms. (c) TGA, and (d) FTIR spectra of $ZnCo_2O_4$, g-C_3N_4 and $ZnCo_2O_4$/g-C_3N_4.
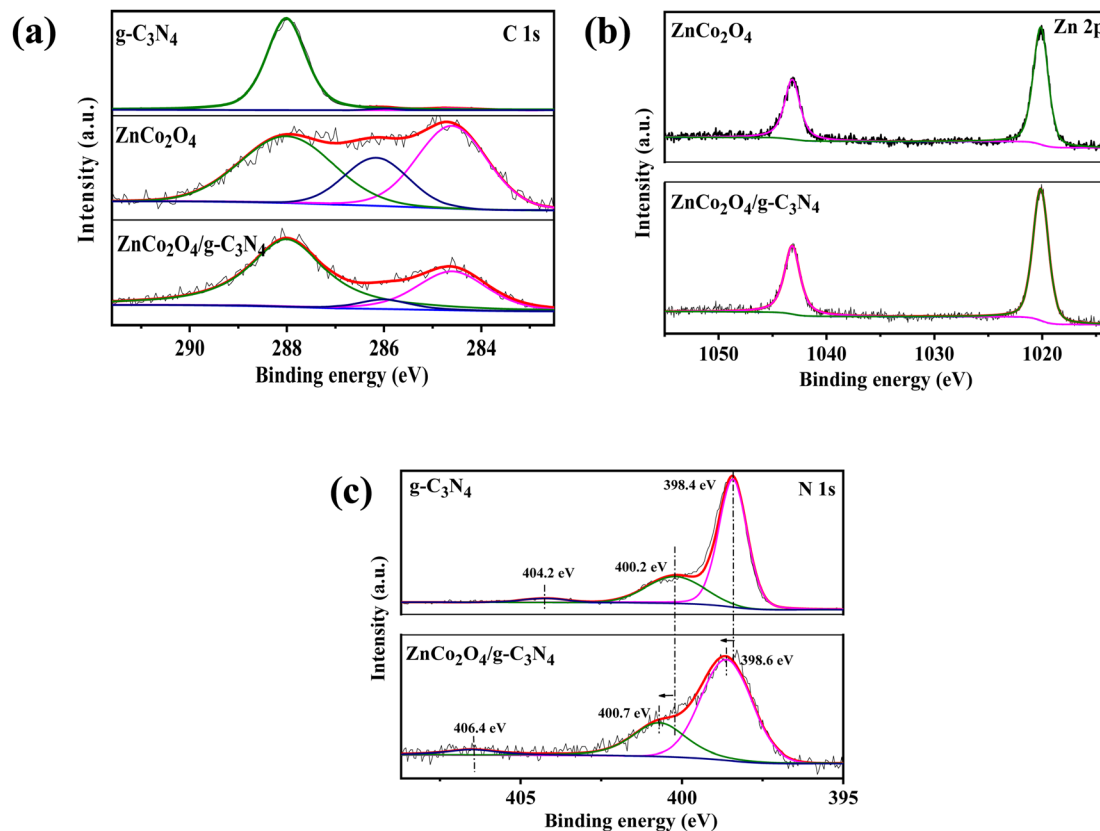
Fig. 3 XPS spectra of (a) C 1s, (b) Zn 2p, and (c) N 1s core levels in several samples.

g-C_3N_4, the surface solvent loss is about 20% at first stage, followed by major weight loss between 500–650 °C reflecting the complete decomposition of g-C_3N_4.[41] In contrast, thermal stability of pure $ZnCo_2O_4$ NPs ranges from 30 to 800 °C. Weight loss occurs at a lower temperature for $ZnCo_2O_4$/g-C_3N_4 than the other two materials due to the combustion of g-C_3N_4 under the catalysis of $ZnCo_2O_4$ on the surfaces. The final weight loss of $ZnCo_2O_4$/g-C_3N_4 at 800 °C reaches ~50%, from which we conclude that the $ZnCo_2O_4$ to g-C_3N_4 weight ratio on the hybrid catalyst is approximate two.

Fig. 2d shows the FTIR spectra of the g-C_3N_4, $ZnCo_2O_4$/g-C_3N_4, and $ZnCo_2O_4$. The stretching vibration mode of C=N and C–N heterocycles is attributed to the broad band in the range of 1200–1800 cm^{-1} for pure g-C_3N_4. The bands at 3000–3500 cm^{-1} are related to the stretching vibration mode of N–H bond, and the –OH group from the surface adsorbed water.[42] All of the g-C_3N_4 vibration bands appear in the $ZnCo_2O_4$/g-C_3N_4 samples, indicating that the g-C_3N_4 structure was preserved during the hybridization process. The peaks in the area from 525 to 725 cm^{-1} are originated from the typical bands of spinel metal oxide and the strong peaks at 568 cm^{-1} and 668 cm^{-1} appear in both pure $ZnCo_2O_4$ and $ZnCo_2O_4$/g-C_3N_4 hybrids.[43]

The chemical states of the samples were investigated by XPS. According to the XPS observations (Fig. 3), C 1s and Zn 2p were found to have undergone no chemical change after loading $ZnCo_2O_4$ on g-C_3N_4. In the C 1s core level analysis, the peak at 284.6 eV was linked to the indefinite carbon adsorbed on the surface or the sp^3 graphitic carbon generated during the polymerization, while the 288.0 eV binding energy belongs to sp^2 hybrid carbon in N–C=N.[44] The signal at 398.4 eV in the N 1s core level analysis of g-C_3N_4 was attributed to the hybrid aromatic nitrogen atom (C–N=C), while the peak of 400.2 eV denotes a tertiary nitrogen (N–$(C)_3$ or C–NH–C) group. Besides, a broad peak of 404.2 eV was generated by π–π excitation between stacked interlayers. However, after $ZnCo_2O_4$ loaded, its chemical state changed to higher bonding energy, indicating that the chemical state of the hybrid aromatic N changed because of the $ZnCo_2O_4$ doping. Specifically, it was reported that the six lone pair electrons in g-C_3N_4 could occupy the free orbit of the center Co atoms to form Co–N, leading in reduced electron density and increased N atom binding energy.[45]

3.2 Catalytic evaluation

The catalytic properties of g-C_3N_4, $ZnCo_2O_4$ and $ZnCo_2O_4$/g-C_3N_4 hybrids in aqueous solution were assessed by the degradation of NOR with the aid of PMS (Fig. 4). All the catalytic experiments were conducted without light irradiation, which thereby avoided the additional energy consumption. The results showed that NOR could be slowly degraded with only PMS and the addition of C_3N_4 could slightly accelerate the removal of NOR. However, the introduction of $ZnCo_2O_4$ can obviously increase the degradation performance of the catalytic oxidation systems. For example, $ZnCo_2O_4$ coupled with PMS could induce a NOR removal rate of 73.6% within 120 min, which is much
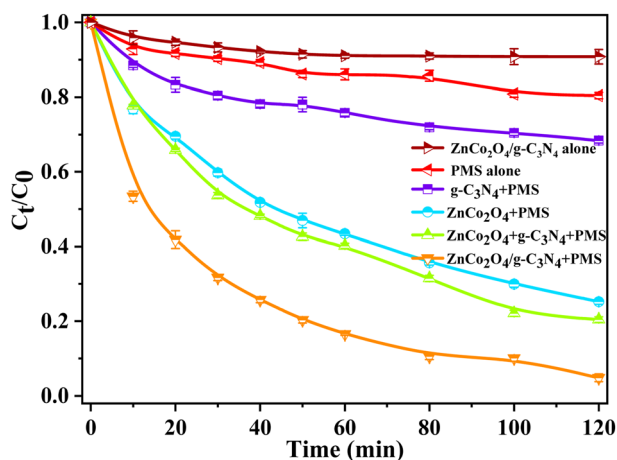
Fig. 4 NOR degradation with different catalysts. (reaction conditions: catalyst = 0.2 g L^{-1}, PMS dosage = 0.15 mM, initial NOR concentration = 0.06 mM, T = 25 °C, without pH adjustment).

higher than those achieved in the above two conditions. In the presence of PMS, ZnCo$_2$O$_4$ and g-C$_3$N$_4$ are physically combined in a 1 : 1 weight ratio, which results in similar removal efficiency of NOR to that of ZnCo$_2$O$_4$. The highest NOR removal rate (~95%) in 120 min was observed for the ZnCo$_2$O$_4$/g-C$_3$N$_4$ coupled with PMS oxidation system, surpassing other counterparts. This performance can be attributed to the built-in electric field in the p–n heterojunction of ZnCo$_2$O$_4$/g-C$_3$N$_4$, in contrast to the simple physical mixture of ZnCo$_2$O$_4$ and g-C$_3$N$_4$.

The effect of surface area on the catalytic performance of catalyst was also surveyed. As confirmed by the BET characterization, the surface area of ZnCo$_2$O$_4$/g-C$_3$N$_4$ catalyst is only somewhat higher than those of pure ZnCo$_2$O$_4$ and g-C$_3$N$_4$ and its specific activity calculated by surface area normalization is also only slightly higher than those of the other two (Table S1†). But the ZnCo$_2$O$_4$/g-C$_3$N$_4$ hybrids possess much higher catalytic activity than the other ones, which implies surface area is not the key factor affecting the catalytic activity. Therefore, the excellent catalytic performance may primarily be credited to the special combination of ZnCo$_2$O$_4$ and g-C$_3$N$_4$, which leads to not only the very stable and uniform dispersion of ZnCo$_2$O$_4$ QDs but

also additional electronic transfer *via* intimate interfacial contact. These thereby enhanced the PMS activation by transition metal.

3.3 Optimization of NOR degradation

3.3.1 Effect of PMS dosage. To investigate the catalytic activities of the samples, control experiments were conducted in terms and the influence of initial PMS concentration on the degradation of NOR by ZnCo$_2$O$_4$/g-C$_3$N$_4$ + PMS system was exemplified. As shown in Fig. 5a, the removal rate of NOR were 62.6%, 73.2%, 95.3%, and 99.1%, respectively, with 0.05, 0.10, 0.15, and 0.20 mM of initial PMS concentration. The increasing concentration of PMS improved the contact of PMS with the surface of the hybrids and attributed to the production of more radicals in general during the reaction, which obviously promoted the degradation of NOR.

3.3.2 Effect of NOR concentration. The effect of initial NOR concentration on its degradation by ZnCo$_2$O$_4$/g-C$_3$N$_4$ + PMS system is shown in Fig. 5b. Higher concentration of NOR led to a lower removal efficiency which decreased from 100% to 73.6% with the NOR concentration increasing from 0.015 mM to 0.12 mM. This may be explained by the increased requirement for active sites on the catalyst surface to generate enough sulfate radical for the decomposition of the more NOR molecule added.

3.3.3 Effect of ZnCo$_2$O$_4$/g-C$_3$N$_4$ dosage. The dosage of ZnCo$_2$O$_4$/g-C$_3$N$_4$ greatly impacted the degradation of NOR and the removal rate increased from 52.6% to 98.3% with the catalyst dosage increasing from 0.1 g L^{-1} to 0.25 g L^{-1} (Fig. 6a). This implied that the increasing amount of ZnCo$_2$O$_4$/g-C$_3$N$_4$ catalyst could generate more active sites for sulfate radical generation. However, increasing from 0.2 g L^{-1} to 0.25 g L^{-1} with the catalyst dosage, may scavenge the radicals through the interaction of extra active sites with sulfate and hydroxyl radicals.

3.3.4 Effect of initial pH value. Fig. 6b shows that the ZnCo$_2$O$_4$/g-C$_3$N$_4$ + PMS system works effectively across a wide initial pH range from 2.95 to 11.04, unlike the traditional homogeneous Fenton reaction, which is significantly impacted by the pH level of the system.[46] The degradation of NOR accelerates considerably with the increasing initial pH value, and reaches the highest rate at 11.04.
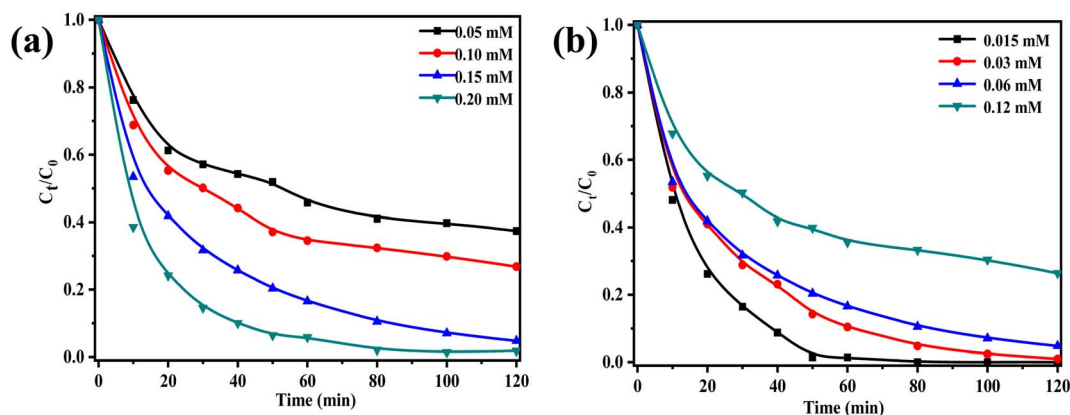

Fig. 5 Comparison the performance of ZnCo$_2$O$_4$/g-C$_3$N$_4$ under different conditions: (a) PMS dosage, (b) initial NOR concentration.
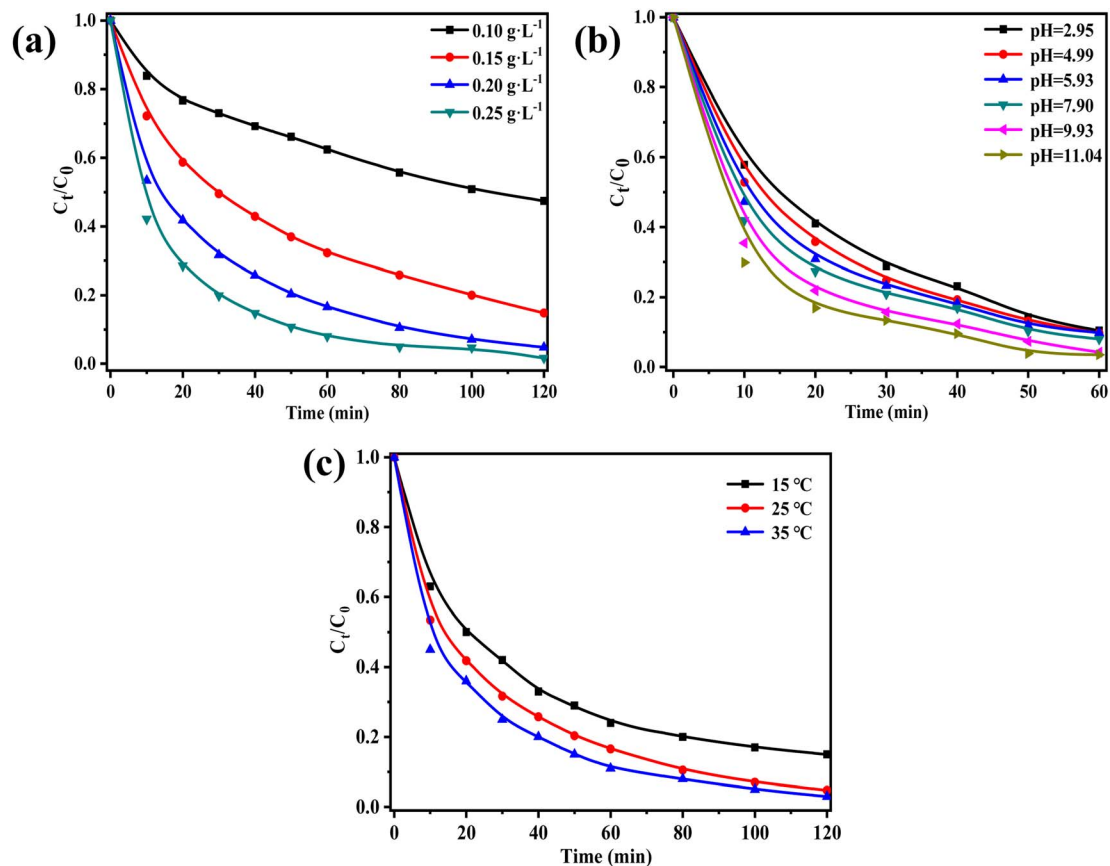
Fig. 6 Comparison the performance of ZnCo$_2$O$_4$/g-C$_3$N$_4$ under different conditions: (a) catalyst dosage, (b) initial pH value, (c) temperature.

The point of zero charge (pH$_{pzc}$) of ZnCo$_2$O$_4$/g-C$_3$N$_4$ was determined to be 5.5 (Fig. S3†). At pH < 5.5, the catalyst surface becomes negatively charged, thus inhibiting the activation of PMS due to electrostatic repulsion between the catalyst and PMS. Conversely, at pH > 5.5 the catalyst becomes positively charged, allowing the adsorption of negatively charged PMS, which in turn results in ROS generation.[47] Furthermore, acidic conditions such as H$^+$ in the system forming hydrogen bonds with O–O in HSO$_5^-$ can slightly inhibit the degradation effect, as it affects the activation of HSO$_5^-$ into active free radicals, thus decreasing the degradation performance.

3.3.5 Effect of initial temperature. It is clear that a rise in temperature is accompanied by an increase in degradation rates, which suggests the catalytic process that produces active radicals is endothermic.[48] This is further illustrated in Fig. 6c, which shows a positive effect within the temperature range of 15–35 °C in the rate of NOR degradation. This is the result of both a heightened rate of persulfate decomposition forming SO$_4^{\bullet-}$, as well as increased collision probability between SO$_4^{\bullet-}$ and CBZ in solution, thereby increasing the NOR degradation rate.[49]

3.4 TOC reduction during reaction and reusability of the ZnCo$_2$O$_4$/g-C$_3$N$_4$ catalyst

Fig. 7a displays the TOC removal and NOR degradation efficiencies for various reaction periods. We found that NOR degradation of 95.3% were achieved after the peroxymonosulfate degradation and the mineralization degree reached 50% after 4 hours of reaction. It can be discovered that the strong oxidizing species (sulfate and hydroxyl radicals) destroyed the majority of the NOR molecules, but that the tiny organic intermediates generated during the catalytic process are not entirely degraded.

The recycled ZnCo$_2$O$_4$/g-C$_3$N$_4$ catalyst demonstrated a good degree of reusability for the degradation of NOR even after four consecutive cycles of testing (Fig. 7b), though its catalytic activity was lower than that of the freshly prepared catalyst. The ability of a catalyst to drive the reduction in activity may be affected by two factors: loss of the catalyst during the recycling process, and a decrease in the catalytic surface area due to the build-up of reaction products on the catalyst surface. In contrast, the ZnCo$_2$O$_4$ catalyst showed a marked reduction in NOR elimination rate from 75% to around 32% after four cycles (Fig. 7c). These findings imply that g-C$_3$N$_4$ support was able to enhance the durability of the ZnCo$_2$O$_4$ catalysts. Furthermore, the Zn and Co ions leaching concentration after reaction were detected. The Zn ion leaching in ZnCo$_2$O$_4$/g-C$_3$N$_4$ system is 0.14 mg L^{-1}, which is lower than that of ZnCo$_2$O$_4$ system (0.55 mg L^{-1}). Whereas, Co ion leaching was not significant, with 0.05 mg L^{-1} and 0.09 mg L^{-1} being measured in ZnCo$_2$O$_4$/g-C$_3$N$_4$ and ZnCo$_2$O$_4$, respectively. The results of the FTIR characterizations before and after use showed that ZnCo$_2$O$_4$/g-
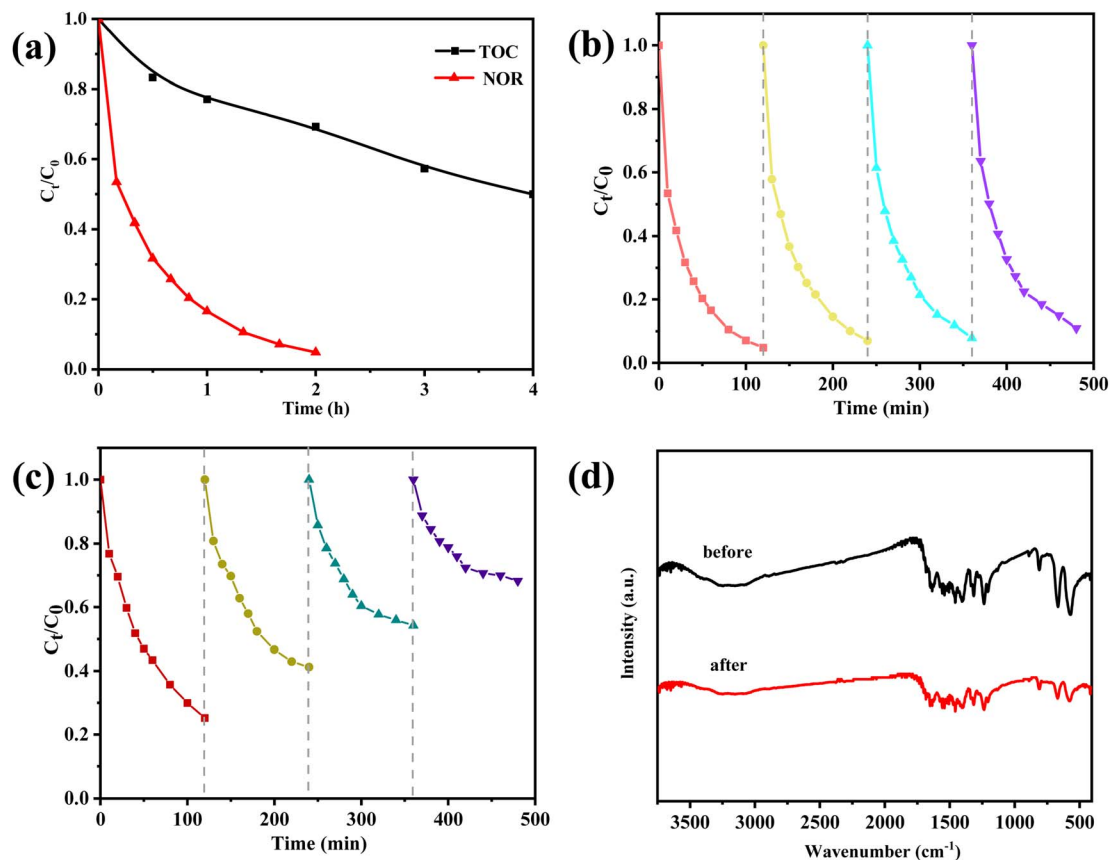
Fig. 7 (a) TOC removal and NOR degradation during the reaction; recycle experiments of NOR removal for (b) $ZnCo_2O_4$/g-C_3N_4 and (c) $ZnCo_2O_4$ catalyst; (d) FTIR spectra of fresh and used $ZnCo_2O_4$/g-C_3N_4 catalyst.

C_3N_4 has an outstanding structural durability, as there was almost no change in the results (Fig. 7d). This observation reflects the good stability of the $ZnCo_2O_4$/g-C_3N_4 catalyst for the activation of PMS, thus confirming its potential for practical applications.

3.5 Mechanism of PMS activation by $ZnCo_2O_4$/g-C_3N_4

In metal-activated PMS system, several types of radicals including $SO_4^{\bullet-}$, $^\bullet OH$, and $SO_5^{\bullet-}$ are commonly generated. Both $SO_4^{\bullet-}$ and $^\bullet OH$ have the potential to attack organic compounds while $SO_5^{\bullet-}$ cannot take part in the reaction due to its poor redox potential (1.1 V *vs.* NHE).[50] To recognize the oxidizing radicals accountable for NOR removal in the $ZnCo_2O_4$/g-C_3N_4 + PMS system, different quenching agents were added to the system (*tert*-butyl alcohol (TBA) for $^\bullet OH$, and ethanol (EtOH) for both $^\bullet OH$ and $SO_4^{\bullet-}$).[51] As shown in Fig. 8a, addition of 500 mM of TBA could achieve obvious decrease of NOR removal (~12%) within 120 min, demonstrating the generation of plenty of $^\bullet OH$ in the catalytic oxidation. Moreover, the NOR removal decreased from ~100% to 73% in 120 min as the same concentration of EtOH was added, which indicated the participation of $SO_4^{\bullet-}$ into the reaction procedure. The presence of alcohols could only partially inhibit the degradation of NOR, possibly due to the fact that they were difficult to cling to the hydrophilic catalyst surface substantially to efficiently capture the surface-adsorbed

radicals. Thus, KI, which may react with surface-bound radicals was utilized to another scavenger to further study the role of radicals for the oxidation degradation of NOR. On this occasion, adding 10 mM of KI significantly reduced the removal rate of NOR to 51%. Based on the above observations, we draw the conclusion that $^\bullet OH$ and $SO_4^{\bullet-}$ are the main reactive species in $ZnCo_2O_4$/g-C_3N_4 activated PMS process, which agrees with recent findings in the literature.[52–54]

Moreover, electron spin resonance (ESR) technique was employed to detect the active radicals in the $ZnCo_2O_4$/g-C_3N_4 + PMS reaction systems. As depicted in Fig. 8b, no DMPO–$^\bullet OH$ and DMPO–$SO_4^{\bullet-}$ adduct was detected when PMS was present alone, indicating that these radicals could not be generated without the existence of catalysts. As expected, characteristic signals of DMPO–$^\bullet OH$ (quarter lines with peak strength of 1 : 2 : 2 : 1, refer to $\alpha_N = \alpha_{\beta-H} = 14.9$ G) and DMPO–$SO_4^{\bullet-}$ (refer to $\alpha_N = 13.2$ G, $\alpha_{\beta-H} = 9.6$ G, $\alpha_{\gamma-H1} = 1.48$ G, $\alpha_{\gamma-H2} = 0.78$ G)[55] adducts were observed in $ZnCo_2O_4$/g-C_3N_4 + PMS system. When reaction time was increased from 5 to 15 min, the peak signals of DMPO–$^\bullet OH$ and DMPO–$SO_4^{\bullet-}$ adducts enhanced, indicating that the amount of reactive species increased during this period.

For the sake of understanding the catalytic reaction mechanism of the $ZnCo_2O_4$/g-C_3N_4 + PMS system, XPS was used to supervise the change in chemical state of the catalyst. Before reaction, XPS spectrum of Co 2p core-level shows typical peaks
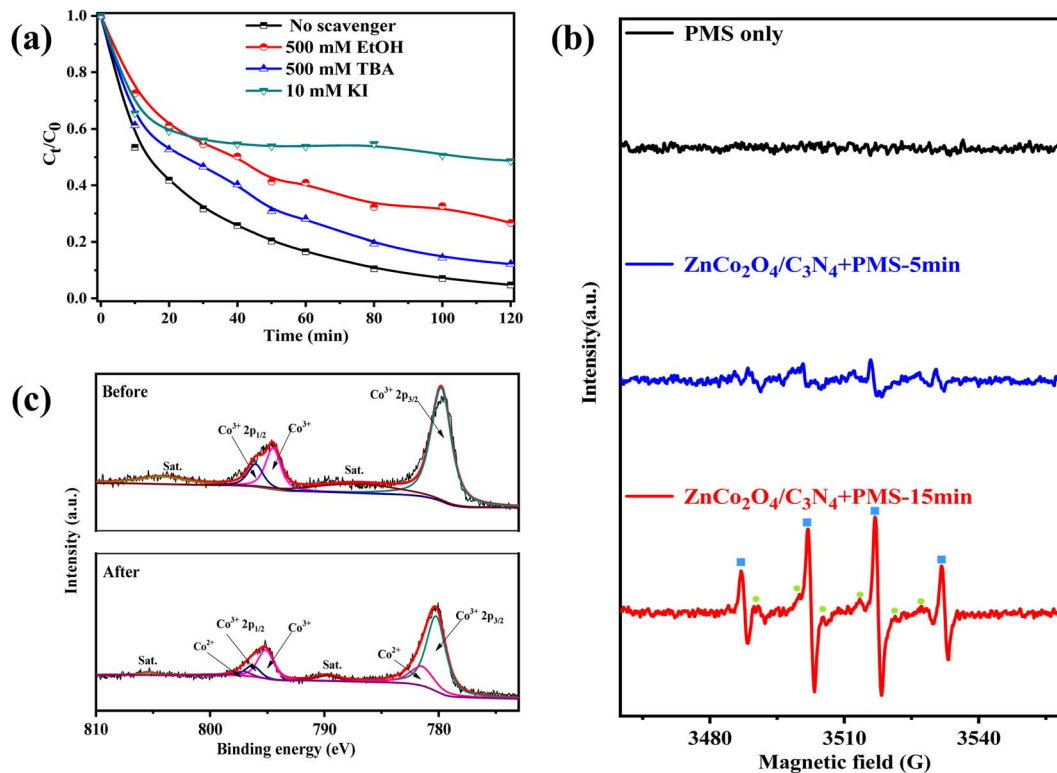
Fig. 8 (a) The quenching experiments using EtOH, TBA, and KI. (b) DMPO−·OH and DMPO−SO$_4$·$^-$ adduct in ESR spectra under different conditions. (c) Co 2p XPS spectrum of ZnCo$_2$O$_4$/g-C$_3$N$_4$ catalyst before and after reaction.
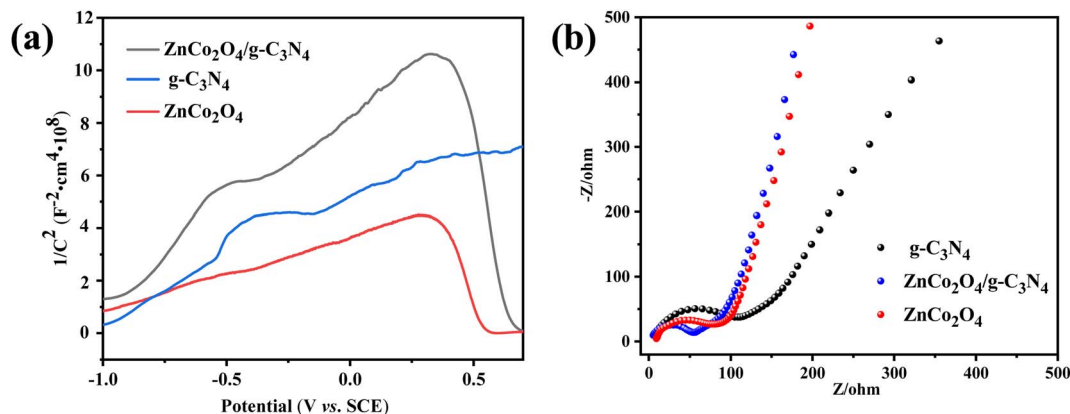

Fig. 9 (a) Mott–Schottky and (b) electrochemical impedance spectroscopy of samples.

at Co respectively, and the peaks at Co 2p$_{3/2}$ and Co 2p$_{1/2}$ slight shift from 779.8 eV to 780.2 eV and from 796.0 eV to 796.3 eV,[56] respectively, after reaction (Fig. 8c). Meanwhile, two new peaks with binding energy at 781.5 eV and 797.1 eV corresponding to Co^{II} appeared, suggesting that the chemical states of some Co species on the catalyst surface were changed in the catalytic process. Three components at 397.4, 398.8 and 399.9 eV in the N 1s XPS spectrum were ascribed to the C–N–C, C–N(–C)–C, and −NH$_x$, respectively (Fig. S4†). Indeed, the relative contribution of −NH$_x$ to the overall N intensity increased from 4% to 11% after the reaction, demonstrating that N sites may also participate in the reaction.

To comprehend the semiconducting characteristics of the catalysts, Mott–Schottky measurements were first conducted under low light conditions on FTO conductive glass. As shown in Fig. 9a, g-C$_3$N$_4$ displays a positive slope, which is consistent with its n-type semiconductor properties. By contrast, ZnCo$_2$O$_4$ exhibits a negative slope, consistent with the p-type semiconductor properties. As for ZnCo$_2$O$_4$/g-C$_3$N$_4$, a typical inverted "V-shape" plot which owns both negative and positive slopes is observed, further confirming the p–n heterojunction of the composite ZnCo$_2$O$_4$/g-C$_3$N$_4$ catalyst.

The electrochemical impedance spectroscopy of the catalysts was also obtained under dark light conditions on the ITO

conductive glass. Normally, smaller arc radii in Nyquist plots reflects stronger capacity transmit charges.[57] As shown in Fig. 9b, the arc radii of $ZnCo_2O_4$/g-C_3N_4 is significantly smaller than those of pure $ZnCo_2O_4$ and g-C_3N_4, suggesting the faster interfacial charge transport. This can be originated from the existence of the internal electric field in the heterojunction interface, which provides more efficient electron transfer during the catalytic reaction.

All in all, a possible reaction mechanism for the degradation of NOR in $ZnCo_2O_4$/g-C_3N_4/PMS system was proposed from the above results as illustrated in Fig. 10. When a $ZnCo_2O_4$/g-C_3N_4 heterojunction is fabricated by tightly bounded p-type $ZnCo_2O_4$ semiconductor with n-type g-C_3N_4 semiconductor, $ZnCo_2O_4$ provides holes to g-C_3N_4 while g-C_3N_4 provides electrons to $ZnCo_2O_4$ in the interface to balance the Fermi level (E_f). Thus, an internal static electric field ($E_{internal}$) is fabricated at the interface with the electric field direction from g-C_3N_4 to $ZnCo_2O_4$. In the case of the catalytic process by $ZnCo_2O_4$/g-C_3N_4 hybrid, a multi-step reaction was involved for PMS activation and NOR degradation, as shown in eqn (1)–(6). According to XPS analysis, $\equiv Co^{II}$ did not exist in $ZnCo_2O_4$/g-C_3N_4 and $ZnCo_2O_4$ catalysts before the reaction, but appeared after the reaction. Furthermore, the control experiment shows that pure g-C_3N_4 hardly exhibit catalytic activity toward the NOR oxidation with PMS and $ZnCo_2O_4$ alone also has a limit catalytic ability. Therefore, the initiation process of the degradation reaction is proposed to be the reaction of HSO_5^- with the variable-valent form $\equiv Co^{III}$ to yield $\equiv Co^{II}$ and $HSO_5^{\cdot-}$ in solution (eqn (1)). When $\equiv Co^{II}$ loses electrons to form $\equiv Co^{III}$, the e^- will quickly pass through the p–n heterojunction to the g-C_3N_4 side due to the internal electric field (eqn (2)). Subsequently, the HSO_5^- reacts with e^- on the side of g-C_3N_4 of the p–n junction interface to generate $\cdot OH$ or $SO_4^{\cdot-}$ (eqn (3) and (4)). The organic molecules are then oxidized by both radicals to produce mineralization products in the last stage (eqn (5) and (6)).
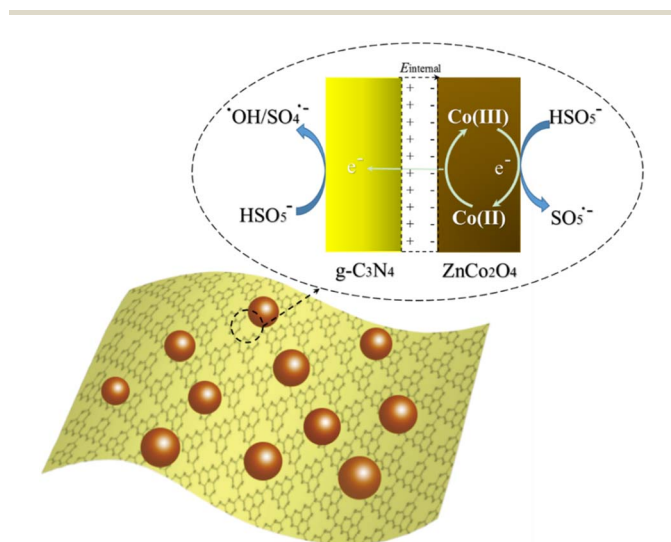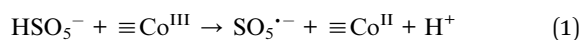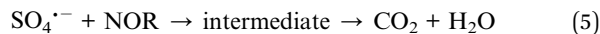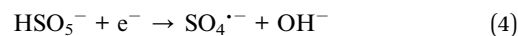
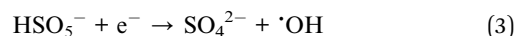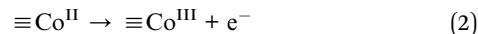$$HSO_5^- + \equiv Co^{III} \rightarrow SO_5^{\cdot-} + \equiv Co^{II} + H^+ \tag{1}$$

Fig. 10 The $ZnCo_2O_4$/g-C_3N_4 p–n junction induced internal electric field facilitates the electron transfer during the activation of PMS.

$$\equiv Co^{II} \rightarrow \equiv Co^{III} + e^- \tag{2}$$

$$HSO_5^- + e^- \rightarrow SO_4^{2-} + \cdot OH \tag{3}$$

$$HSO_5^- + e^- \rightarrow SO_4^{\cdot-} + OH^- \tag{4}$$

$$SO_4^{\cdot-} + NOR \rightarrow intermediate \rightarrow CO_2 + H_2O \tag{5}$$

$$\cdot OH + NOR \rightarrow intermediate \rightarrow CO_2 + H_2O \tag{6}$$

3.6 Identification of intermediates and transformation pathways

Based on the knowledge from prior literature and the fragmentation patterns acquired from liquid chromatography-mass spectrometry analysis (HPLC–QqQ–MS/MS), the structures of the intermediate products were tentatively determined.[58–60] A total of 8 intermediates were detected during the degradation of NOR with $ZnCo_2O_4$/g-C_3N_4 + PMS system containing protonated ions ([M + H]$^+$), as well as the proposed molecular structure and mass spectra were presented in Fig. S5.† For MS/MS analyses of these products, specific parameters are supplied in Table S2.†

In reality, many of the oxidation processes, such as ozonation, photocatalysis, and thermally activated PMS, had already been identified in other AOPs. As previously indicated, when $SO_4^{\cdot-}$ or $\cdot OH$ radical dots predominated the process, the degradation mechanisms were noticeably different. For example, the attack of NOR by $SO_4^{\cdot-}$ would form NOR radical dots firstly through electron transfer reactions which subsequently produced ($\cdot OH$) NOR radicals by the hydroxyl abstraction or addition reaction when combined with H_2O. While $\cdot OH$ would be likely to attack the carbon–carbon double bond next to the carboxylic acid group.[61] When both the piperazinyl and quinolone moieties of NOR were attacked by either sulfate or hydroxyl radicals simultaneously, NOR would be degraded through multiple routes because of the concurrent oxidations of various reactive sites in the parent molecules. Despite of the complexity, prevalent degradation pathways were hypothesized based on the detected intermediates, in which defluorination, transformations of quinolone and piperazinyl groups simultaneously or successively, occurred. As shown in Fig. 11, there are three main pathways in this reaction.

3.6.1 Pathway 1: piperazinyl ring transformation. In the pathway I, the piperazinyl ring in NOR was attacked by radicals, producing the intermediates with the protonated forms at m/z 352, and 252. What's more, the detected product 9 (m/z 168) might be the further decay form. The fragmentation ions from the product 1 and 2 were demonstrated in Fig. S5.†

3.6.2 Pathway 2: defluorination. Then after, product 3 (m/z 318) was generated *via* the pathway II, another process named defluorination reaction occurring on NOR. The product was proved by five product ions at m/z 300 (−18 Da), 298 (−20 Da), 277 (−41 Da), 274 (−20−28 Da), and 245 (−20−28−29 Da), related to the loss of H_2O (18 Da), HF (20 Da), CO (28 Da), C_2H_5O (41 Da), CH_2CH_3 (29 Da), respectively.
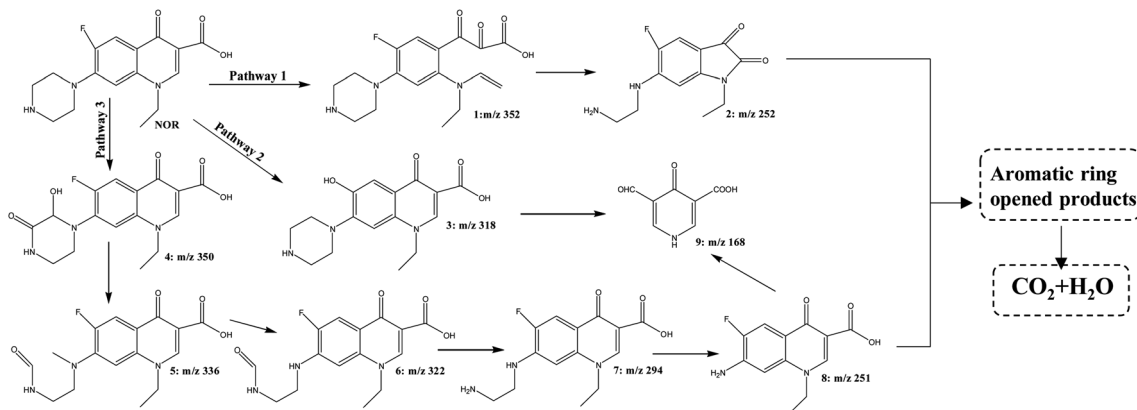
Fig. 11 Proposed partial degradation pathway of NOR in ZnCo$_2$O$_4$/g-C$_3$N$_4$+PMS system.

3.6.3 Pathway 3: quinolone group transformation. According to pathway III, product 4 with protonated form at m/z 350 (+2O) was probably created after oxidation reaction, followed by the generation of the products with protonated form at m/z 336 (−O), 322 (−CH$_2$), 294 (−CO), and 251 (−CH$_5$N + O−CO), decaying step by step, respectively. In this case, opening the ring of product 4 led to the development of product 5 (m/z 336) which was subsequently transformed into product 6 (m/z 322) by the loss of CH$_2$ group immediately. Moreover, product 9 (m/z 168) might be the further product whose ions were proved from the previous research to validate the intermediates.

However, some products in this system were not detected probably owing to the weak response or the low concentration. Lack of relevant standards to determine the actual concentrations, ion counts associated with each individual degradation product were normalized according to the initial concentration of the parent antibiotics. This method was used to estimate the yields and the evolution of degradation products.

4. Conclusion

Plenty of ultrafine ZnCo$_2$O$_4$ QDs were anchored onto the g-C$_3$N$_4$ nanosheets tightly through *in situ* growth during a facile hydrothermal process to achieve ZnCo$_2$O$_4$/g-C$_3$N$_4$ p–n heterojunction which was employed to the PMS activation for NOR degradation. The degradation of NOR was significantly promoted due to the synergistic effect between ZnCo$_2$O$_4$ and g-C$_3$N$_4$ for PMS activation. The built-in electric field in the ZnCo$_2$O$_4$/g-C$_3$N$_4$ hybrid facilitated the electron transfer and the large specific surface area originated from the ultrafine ZnCo$_2$O$_4$ NPs also provided lots of catalytic activity sites and improved the diffusion of chemically active species. According to a free radical quenching experiments and ESR detection, the main oxidizing species in degradation reactions were SO$_4^{\bullet-}$ and $^{\bullet}$OH. This proposed ZnCo$_2$O$_4$/g-C$_3$N$_4$ + PMS system can be used for the elimination of antibiotic pollution of water.

Author contributions

Tao Zeng: writing – review & editing, funding acquisition. Sijia Jin: investigation, writing – original draft. Zhiquan Jin: data curation, formal analysis. Shuqi Li: methodology, formal analysis. Rui Zou: investigation. Xiaole Zhang: writing – review & editing, funding acquisition. Shuang Song: supervision. Min Liu: validation, writing – review & editing.

Conflicts of interest

The authors declare that they have no known competing financial interests or personal relationships that could have appeared to influence the work reported in this paper.

Acknowledgements

References

1 Y. L. Luo, W. S. Guo, H. H. Ngo, L. D. Nghiem, F. I. Hai, J. Zhang, S. Liang and X. C. C. Wang, *Sci. Total Environ.*, 2014, **473**, 619–641.

2 A. Wang, H. Wang, H. Deng, S. Wang, W. Shi, Z. Yi, R. Qiu and K. Yan, *Appl. Catal., B*, 2019, **248**, 298–308.

3 C. Liu, V. Nanaboina, G. V. Korshin and W. Jiang, *Water Res.*, 2012, **46**, 5235–5246.

4 V. T. Nguyen, T. D. H. Vo, T. B. Nguyen, N. D. Dat, B. T. Huu, X. C. Nguyen, T. Tran, T. N. C. Le, T. G. H. Duong, M. H. Bui, C. D. Dong and X. T. Bui, *Chemosphere*, 2022, **288**, 132577.

5 C. L. Amorim, A. S. Maia, R. B. R. Mesquita, A. O. S. S. Rangel, M. C. M. van Loosdrecht, M. E. Tiritan and P. M. L. Castro, *Water Res.*, 2014, **50**, 101–113.

6 H. Wu, X. Niu, J. Yang, C. Wang and M. Lu, *Chem. Eng. J.*, 2016, **294**, 410–416.

7 T. K. Das, S. Remanan, S. Ghosh and N. C. Das, *J. Environ. Chem. Eng.*, 2021, **9**, 104596.

8 T. K. Das and N. C. Das, *Int. Nano Lett.*, 2022, **12**, 223–242.

9 T. K. Das, S. Remanan, S. Ghosh, S. K. Ghosh and N. C. Das, *Environ. Nanotechnol., Monit. Manage.*, 2021, **15**, 100411.

10 M. J. Hülsey, C. W. Lim and N. Yan, *Chem. Sci.*, 2020, **11**, 1456–1468.

11 A. Moores and N. Yan, *ACS Sustainable Chem. Eng.*, 2017, **5**, 11124.

12 T. Wang, X. Cao and L. Jiao, *Carb. Neutrality*, 2022, **1**, 21.

13 W. D. Oh, Z. L. Dong and T. T. Lim, *Appl. Catal., B*, 2016, **194**, 169–201.

14 Q. F. Wang, Y. S. Shao, N. Y. Gao, W. H. Chu, J. X. Chen, X. Lu, Y. P. Zhu and N. An, *Sep. Purif. Technol.*, 2017, **189**, 176–185.

15 G. P. Anipsitakis and D. D. Dionysiou, *Environ. Sci. Technol.*, 2004, **38**, 3705–3712.

16 J. Bai, X. Li, G. Liu, Y. Qian and S. Xiong, *Adv. Funct. Mater.*, 2014, **24**, 3012–3020.

17 T. W. Kim, M. A. Woo, M. Regis and K. S. Choi, *J. Phys. Chem. Lett.*, 2014, **5**, 2370–2374.

18 Z. Q. Liu, H. Cheng, N. Li, T. Y. Ma and Y. Z. Su, *Adv. Mater.*, 2016, **28**, 3777–3784.

19 X. Li, L. Zhao, C. Shao, X. Li, W. Sun and Y. Liu, *J. Colloid Interface Sci.*, 2018, **530**, 345–352.

20 N. Liu, Z. Y. Duan, Q. Q. Zhang and J. Q. Guan, *Chem. Eng. J.*, 2021, **419**, 129567.

21 X. L. Zhang, N. Wang, L. L. Geng, J. N. Fu, H. Hu, D. S. Zhang, B. Y. Zhu, J. Carozza and H. X. Han, *J. Colloid Interface Sci.*, 2018, **512**, 844–852.

22 S. Shrestha, B. Wang and P. Dutta, *Adv. Colloid Interface Sci.*, 2020, **279**, 102162.

23 Y. P. Qiu, Q. Shi, W. Z. Wang, S. H. Xia, H. Dai, H. Yin, Z. Q. Yang and P. Wang, *Small*, 2022, 2106143, DOI: **10.1002/smll.202106143**.

24 Z. P. Ma, C. Tsounis, C. Y. Toe, P. V. Kumar, B. Subhash, S. B. Xi, H. Y. Yang, S. J. Zhou, Z. H. Lin, K. H. Wu, R. J. Wong, L. Thomsen, N. M. Bedford, X. Y. Lu, Y. H. Ng, Z. J. Han and R. Amal, *ACS Catal.*, 2022, **12**, 4792–4805.

25 F. Z. Song, Q. L. Zhu, X. C. Yang, W. W. Zhan, P. Pachfule, N. Tsumori and Q. Xu, *Adv. Energy Mater.*, 2018, **8**, 1701416.

26 W. J. Shao, C. He, M. Zhou, C. D. Yang, Y. Gao, S. Li, L. Ma, L. Qiu, C. Cheng and C. S. Zhao, *J. Mater. Chem. A*, 2020, **8**, 3168–3179.

27 F. Y. Xiao, H. Ren, H. S. Zhou, H. Z. Wang, N. Wang and D. W. Pan, *ACS Appl. Nano Mater.*, 2019, **2**, 5420–5429.

28 C. Wang, P. Shi, X. Cai, Q. Xu, X. Zhou, X. Zhou, D. Yang, J. Fan, Y. Min, H. Ge and W. Yao, *J. Phys. Chem. C*, 2016, **120**, 336–344.

29 Y. Li, S. Ma, S. Xu, H. Fu, Z. Li, K. Li, K. Sheng, J. Du, X. Lu, X. Li and S. Liu, *Chem. Eng. J.*, 2020, **387**, 124094.

30 H. Li, C. Shan and B. Pan, *Sci. Total Environ.*, 2019, **675**, 62–72.

31 H. Liu, Z. He, J. Li and S. Zhao, *Chem. Eng. J.*, 2023, **451**, 138597.

32 N. Y. Cheng, J. Q. Tian, Q. Liu, C. J. Ge, A. H. Qusti, A. M. Asiri, A. O. Al-Youbi and X. P. Sun, *ACS Appl. Mater. Interfaces*, 2013, **5**, 6815–6819.

33 J. Q. Tian, Q. Liu, C. J. Ge, Z. C. Xing, A. M. Asiri, A. O. Al Youbi and X. P. Sun, *Nanoscale*, 2013, **5**, 8921–8924.

34 J. Y. Qin and H. P. Zeng, *Appl. Catal., B*, 2017, **209**, 161–173.

35 C. Wan, L. Zhou, L. Sun, L. X. Xu, D. G. Cheng, F. Q. Chen, X. L. Zhan and Y. R. Yang, *Chem. Eng. J.*, 2020, **396**, 125229.

36 H. Wang, R. Niu, J. Liu, S. Guo, Y. Yang, Z. Liu and J. Li, *Nano Res.*, 2022, **15**, 6987–6998.

37 J. W. Liu, J. G. Jiang, Y. Meng, A. Aihemaiti, Y. W. Xu, H. L. Xiang, Y. C. Gao and X. J. Chen, *J. Hazard. Mater.*, 2020, **388**, 122026.

38 G. Huang, F. Zhang, X. Du, Y. Qin, D. Yin and L. Wang, *ACS Nano*, 2015, **9**, 1592–1599.

39 Y. Li, K. Lv, W. Ho, F. Dong, X. Wu and Y. Xia, *Appl. Catal., B*, 2017, **202**, 611–619.

40 X. Guo, L. Ding, K. Kanamori, K. Nakanishi and H. Yang, *Microporous Mesoporous Mater.*, 2017, **245**, 51–57.

41 Y. Su, P. Chen, F. Wang, Q. Zhang, T. Chen, Y. Wang, K. Yao, W. Lv and G. Liu, *RSC Adv.*, 2017, 7, 34096–34103.

42 X. Wang and Z. Nan, *Sep. Purif. Technol.*, 2020, **233**, 116023.

43 C. R. Mariappan, R. Kumar and G. Vijaya Prakash, *RSC Adv.*, 2015, **5**, 26843–26849.

44 Z. Bao, M. Xing, Y. Zhou, J. Lv, D. Lei, Y. Zhang, J. Cai, J. Wang, Z. Sun, W. Chen, X. Gan, X. Yang, Q. Han, M. Zhang, J. Dai and Y. Wu, *Adv. Sustainable Syst.*, 2021, **5**, 2100087.

45 H. Li, C. Shan and B. Pan, *Environ. Sci. Technol.*, 2018, **52**, 2197–2205.

46 Y. Gao, Y. Rao, H. Ning, J. Chen, Q. Zeng, F. Tian and N. Gao, *Sep. Purif. Technol.*, 2022, **297**, 121555.

47 W. Zheng, Y. Sun and Y. Gu, *J. Hazard. Mater.*, 2022, **436**, 129058.

48 C. Wang, J. Kim, M. Kim, H. Lim, M. Zhang, J. You, J.-H. Yun, Y. Bando, J. Li and Y. Yamauchi, *J. Mater. Chem. A*, 2019, 7, 13743–13750.

49 W.-C. Yun, K.-Y. A. Lin, W.-C. Tong, Y.-F. Lin and Y. Du, *Chem. Eng. J.*, 2019, **373**, 1329–1337.

50 W. D. Oh, Z. Dong and T. T. Lim, *Appl. Catal., B*, 2016, **194**, 169–201.

51 C. Zhu, F. Zhu, D. D. Dionysiou, D. Zhou, G. Fang and J. Gao, *Water Res.*, 2018, **139**, 66–73.

52 Z. Y. Li, Y. L. Liu, P. N. He, X. Zhang, L. Wang, H. T. Gu, H. C. Zhang and J. Ma, *Chem. Eng. J.*, 2021, **418**, 129464.

53 Z. Wang, W. Qiu, S. Pang, Y. Gao, Y. Zhou, Y. Cao and J. Jiang, *Water Res.*, 2020, **172**, 115504.

54 Z. Yang, Y. Li, X. Zhang, X. Cui, S. He, H. Liang and A. Ding, *Chem. Eng. J.*, 2020, **384**, 123319.

55 T. Liu, K. Wu, M. Wang, C. Jing, Y. Chen, S. Yang and P. Jin, *Chemosphere*, 2021, **262**, 127845.

56 H. Y. Chen and P. C. Chen, *Appl. Surf. Sci.*, 2020, **505**, 144460.

57 X. Feng, P. Wang, J. Hou, J. Qian, C. Wang and Y. Ao, *Chem. Eng. J.*, 2018, **352**, 947–956.

58 Y. Fan, Y. R. Liu, X. Hu and Z. R. Sun, *Chemosphere*, 2021, **275**, 130059.

59 L. W. Chen, X. Zuo, S. J. Yang, T. M. Cai and D. H. Ding, *Chem. Eng. J.*, 2019, **359**, 373–384.

60 B. M. Liu, W. B. Song, H. X. Wu, Z. Y. Liu, Y. Teng, Y. J. Sun, Y. H. Xu and H. L. Zheng, *Chem. Eng. J.*, 2020, **398**, 125498.

61 C. Liu, V. Nanaboina, G. V. Korshin and W. J. Jiang, *Water Res.*, 2012, **46**, 5235–5246.